Numerical Study of Bi-axial Cross-flow Turbine

Quentin Clémençot, Pierre-Luc Delafin, Thierry Maître

Numerical Study of Bi-axial Cross-flow Turbine

Q. Clémençot, P.-L. Delafin and T. Maître

***Abstract*—A bi-axial cross-flow water turbine is numerically simulated to evaluate its performance with a view to carrying out experiments on a prototype. Two axes of rotation and a chain-pulley system allow for an innovative blade kinematics. Indeed, the angle of attack of the blades is constant over a portion of their trajectory. This is a sought-after characteristics but difficult to obtain for conventional cross-flow turbines. 2D URANS k-ω SST simulations are carried out. Experimental data from an oscillating airfoil case are used to validate the numerical simulation process. The impact of solidity for one-blade turbine and the impact of the number of blades at iso-solidity are studied. The unbalance performance between the upstream and downstream parts of the turbine are also investigated.**

***Index Terms*—bi-axial turbine , CFD, cross-flow turbine, marine renewable energy, OpenFOAM, overset mesh**

I. Introduction

DARRIEUS turbines are named after their inventor, Georges Darrieus, a French engineer who patented them in 1931 [1]. This type of turbine has been widely studied in recent decades [2]–[5]. Their main particularity is to have an axis of rotation perpendicular to the current. This allows the turbine to have a rectangular swept area, making it particularly suitable for use on rivers, for example. But this particularity brings two obstacles to improving their performance: a non-constant angle of attack and half a revolution where blades travel in the wake of the upstream part of the turbine.

Even at constant rotational speed and constant upstream fluid velocity, the angle of attack of the blades (α) with respect to the relative speed of the fluid varies over a revolution (fig. 1). In order to simplify, α is classically calculated with the undisturbed upstream velocity. Under this assumption, α is a function of the blade angular position θ and $\lambda = V/U_\infty$, the ratio between the speed of the blades with respect to the fixed reference frame V, and the fluid speed far upstream U_∞. The speed of a blade is given by the product of the turbine rotational speed ω and the turbine radius r: $V = \omega \times r$. Equation (1) gives an approximation of the relation between these parameters.

$$\alpha = \arctan \frac{\sin\theta}{\cos\theta + \lambda} \tag{1}$$

However, this equation that can be found in the literature [6] is based on a very strong simplification so that the predicted angle of attack can be quite different from the actual angle of attack. Firstly, the main velocity component decreases when approaching the turbine, leading to an angle of attack smaller than the one calculated using equation (1). Secondly, to have a better approximation of the angle of attack, it is important to take into account the effects related to the dynamics of the blade. Migliore [7] showed that the flow curvature effects on a Darrieus turbine create in particular a virtual incidence that shifts to the left the lift curve of blade. Moreover, in the downstream part of their trajectory, i.e. $\theta \in [180°, 360°]$, the blades evolve in the wake created by their passage in the upstream part, i.e. $\theta \in [0°, 180°]$. The variation of angle of attack in the upstream part may cause it to exceed the stall angle, leading to eddies creation and their advection in the wake of the blades. Therefore, the angle of attack is hard to predict in the downstream part of the trajectory and the power coefficient in this zone is lower than in the upstream part. These difficulties are not encountered by horizontal axis turbines (HAT), so their performances is still higher than cross-flow turbines [8]. In an attempt to overcome the limitations of classic cross-flow turbines, several possibilities are being explored. Passive or active variable pitch control technologies, for example, have led to an increase in efficiency. The blades are no longer fixed in the turbine frame but have a degree of freedom in their angular position. Delafin et al. [9] find an active pitching law allowing a 40% increase in the power coefficient together with a better balance in torque generation between the upstream and downstream parts. Even more disruptive innovations, moving away from the Darrieus turbines, are also envisaged in the world of cross-flow turbines. In the early 1980s, McKinney [10] described

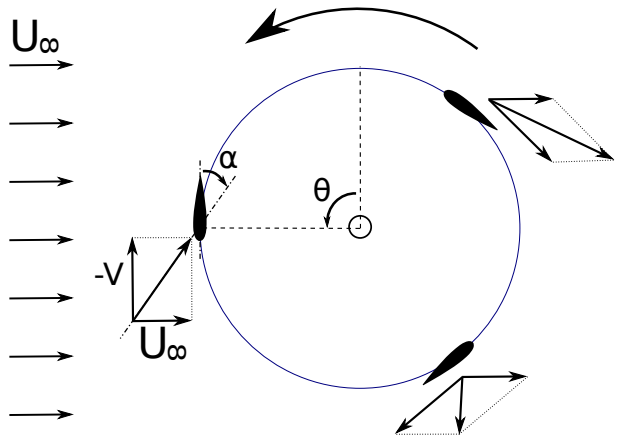

Fig. 1. Scheme of a 3-blades Darrieus turbine and evolution of the geometrical angle of attack.

Q. Clémençot (e-mail: quentin.clemencot@univ-grenoble-alpes.fr), P.-L. Delafin and T. Maître are with Univ Grenoble Alpes, CNRS, Grenoble INP, LEGI, 38000 Grenoble, France.

and experimentally tested a single oscillating wing system with simultaneous hammering and pitching motions, capable of extracting energy from the flow. In this configuration, the blade see only unperturbed upstream flow and never work in its own wake. Kinsey [11] used CFD tools to improve the performance of this turbine and achieve attractive efficiency.

The turbine presented here is considered to partially overcome the non-constant angle of attack issue of cross-flow turbines by adopting two axes of rotation and a chain-pulley system (fig. 2). This design allows a perpendicular translation of the blades with respect to the upstream velocity on two portions of the trajectory. Naccache [12], [13] performed a 3D Unsteady-RANS study on a single-blade turbine of this kind and obtained a promising power coefficient: Cp = 0.4. The aim of this study is to better understand the influence of both solidity and number of blades on the performance of the turbine.

II. Turbine and flow characteristics

A. General description

As represented in fig. 2, the blades are arranged at regular intervals along two chains, themselves connected to pulleys of the same radius r. The pulleys are placed so as to form two rotation axes orthogonal to the upstream flow velocity. Parameter h designates the distance between the axes. The total turbine height is therefore $d = h + 2r$ and the distance travelled by the blades during one revolution is $l = 2h + 2\pi r$. Considering b the blade span, the projected area of the turbine is a rectangle of area $S = b \times (h + 2r)$. All turbines simulated in this study have an aspect ratio $h/r = 4$. The dimensions of the turbine are summarized in Table I.

One-blade, two-blade and three-blade turbines are simulated. Three different chord lengths are used: $c/r = 0.8$, $c/r = 0.4$ and $c/r = 0.266$. This makes it possible, in particular, to study the influence of the number of blades with a constant solidity ($\sigma = N \times c/l$).

TABLE I
Summary of turbine dimensions

parameter	definition	dimension
h	distance between the axes of the pulleys	40cm
r	pulleys radius	10cm
b	blade span	1m (2D) 8cm
c	blade chord	8/2=4cm 8/3=2.66cm

In order to get closer to the experimental test conditions, the simulations are not carried out at iso-Reynolds. The kinematic viscosity of the fluid is that of water, i.e. $\nu = 10^{-6} m^2.s^{-1}$. Taking the relative velocity of the fluid during the upstream vertical translation, $W = U_\infty \times \sqrt{1 + \lambda^2}$, as the reference velocity, the Reynold number varies between $Re = 8.43 \times 10^4$ (the shortest chord length and the lowest λ) and $Re = 4.07 \times 10^5$ (the longest chord length and the highest λ).

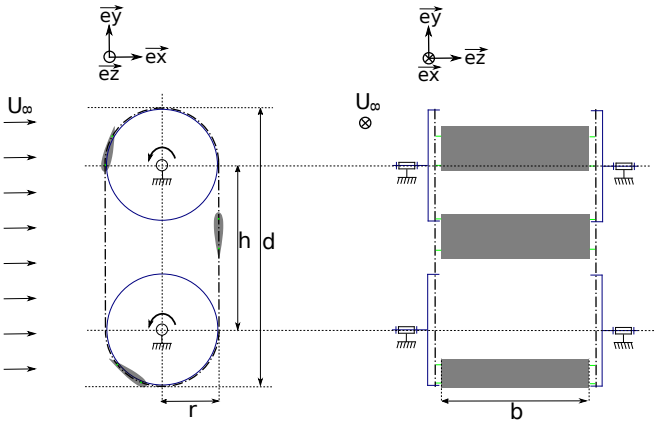

Fig. 2. Scheme of a 3-blades bi-axial turbine

B. Blade kinematics

The blades are NACA 0012 symmetrical profiles. There are two kinematic connection points (A and B) between a blade and the chain (fig. 3). These points are located at $x_A/c = 1/8$ and $x_B/c = 7/8$ of the leading edge respectively. The kinematic link at point A, close to the leading edge, is a pivot of axis $(A, \vec{e_z})$. The kinematic link at point B is closer to the trailing edge. It allows z-axis rotation and translation along the chord line. Points A and B will pass through the same points in space during a turbine revolution. During one revolution, a blade will thus successively have an upstream translation movement directed downwards, a rotation around the lower pulley (semicircle), a downstream translation directed upwards and finally a rotation around the upper pulley (semicircle). The blades are therefore either in translation, in rotation or in a more complex transition movement between these two states (fig. 3). The transition takes place when the attachment points A and B are not on the same rectilinear or circular portion. This transition avoids a theoretical discontinuity in the blade rotational speed. Indeed, with a rigid attachment at a single point, the blade rotation speed would be a step function of time passing instantaneously from 0 to ω. And according to the mechanics of non-deformable solids, this infinite angular acceleration would imply an infinite torque. In practice, the blade would be subject to a strong mechanical stress 4 times per revolution. A two-point fixing solution seems more interesting for the durability of the turbine.

C. Hydraulic power coefficient

The instantaneous power transmitted by the fluid to the blade is equal to the product of the mechanical action tensor by the kinematic tensor expressed at the same point. When writing this relation at point A comes equation (2).

$$P(t) = \overrightarrow{F}_{f \to b}(t).\overrightarrow{V}_{A \in b/\mathcal{R}_0}(t) + \overrightarrow{M}_{A, f \to b}(t).\overrightarrow{\omega}_{b/\mathcal{R}_0}(t) \quad (2)$$

In equation (2), P is the power received by the blade in W. $\overrightarrow{F}_{f \to b}$ is the force exerted by the fluid on the blade in N. $\overrightarrow{V}_{A \in b/\mathcal{R}_0}$ is the velocity of point A

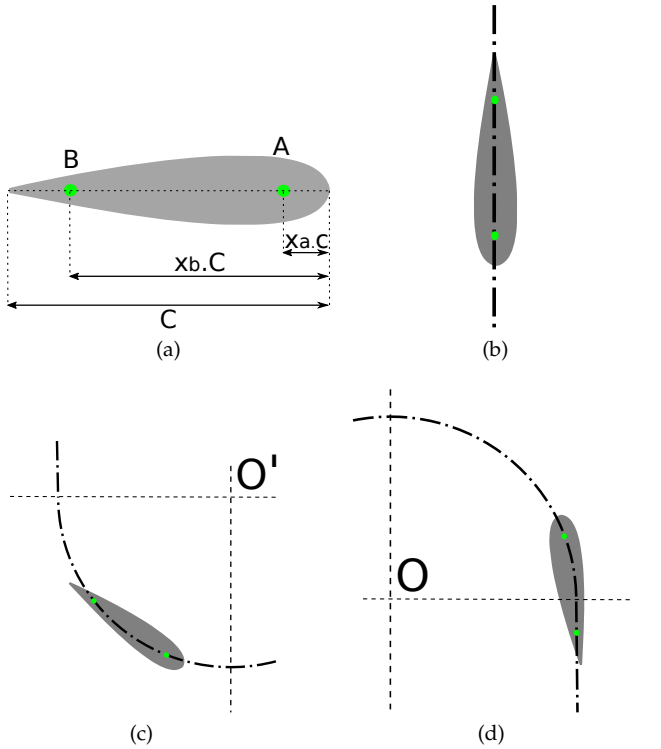

Fig. 3. Point A and B of kinematic connections between the blade and the chain and their dimensionless distance from the leading edge (a). Examples of three kinematic states of the blade: a pure translation (b), a pure rotation around the lower pulley axis (c) and a composite kinematics of translation and rotation (d).

belonging to the blade with respect to the fixed frame of reference in $m.s^{-1}$. $\overrightarrow{M}_{A,f\to b}$ is the moment exerted by the fluid on the blade calculated at point A in $N.m$. Finally, $\overrightarrow{\omega}_{b/\mathcal{R}_0}$ is the rotation speed of the blade with respect to the fixed reference frame in $rad.s^{-1}$.

To lighten the notations, the value taken by a time function ϕ at time t will be noted $\phi(t) = \phi$. Its temporal average will be noted $\overline{\phi}$. The instantaneous power coefficient received by the blade i is equal to the ratio between the captured power and the kinetic power of the fluid passing through the projected surface in the absence of the turbine, as in equation (3).

$$C_{p,i} = \frac{P_i}{\frac{1}{2}\rho U_\infty^3 db} \tag{3}$$

In the case of a multi-blade turbine, the total instantaneous power coefficient is given by the sum of the contributions of the blades, as in equation (4).

$$C_{p,tot} = \sum_i C_{p,i} \tag{4}$$

III. Numerical simulation

A. Simulation setting

The flow is modelled by the incompressible 2D Unsteady Reynolds Averaged Navier–Stokes equations (URANS). Discretization and resolution are done by the finite volume solver OpenFOAM v2012. The Shear Stress Transport (SST) $k-\omega$ turbulence model is used to close the system of equations. This model uses a blending function to switch from $k-\omega$ turbulence modeling for regions close to a wall to $k-\epsilon$ modeling for the rest of the simulation domain [14]. This model is widely used in research and in industry [15]. It allows in particular a good prediction of the flow in the presence of an adverse pressure gradient. One of its limitations is that it assumes a totally turbulent boundary layer, contrary to a transition model of type $k-kl-\omega$ for example.

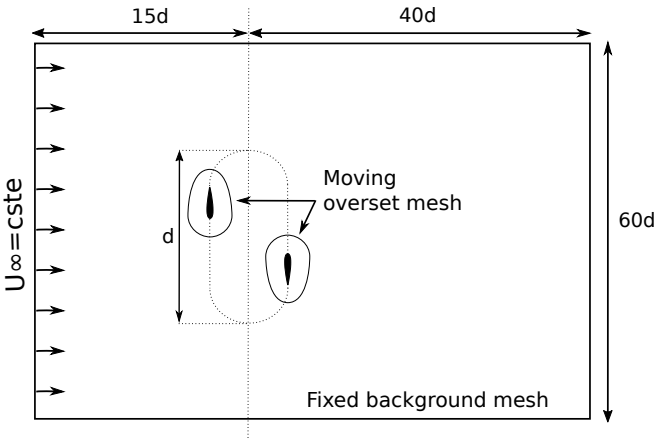

Fig. 4. Simulation domain.

B. Domain & mesh

The rectangular simulation domain extends over a length of 55d and a height of 60d (fig. 4). Symmetry plane boundary conditions are applied on the upper and lower borders. At the entry of the domain, a uniform velocity is imposed $U_\infty = 1m.s^{-1}$ with a turbulent intensity $I = 8\%$. A zero-gradient condition is imposed for the pressure. At the exit of the domain, a uniform pressure is imposed.

The motion of the blades in the simulation domain is made possible by the use of an overset mesh. Two types of meshes are used. A first fixed background mesh extends over the entire simulation domain and at the boundaries of which boundary conditions are imposed. Each blade is surrounded by an overset mesh which is superimposed on the background mesh and follows the blade motion (fig. 4). Both types of meshes exchange information by interpolation. The cells at the border of the overset calculate the values of their field by interpolation with the closest background cells (fig. 5). Some background mesh cells that are under an overset mesh are disabled. A background cell adjacent to a disabled cell calculates the value of its fields by interpolation with the overset mesh. The inverse distance method is used for interpolation. The behaviour of this type of mesh is summarized for a 1D case in fig. 6. This meshing method is more flexible to use than an Arbitrary Mesh Interface (AMI) since it allows to impose any trajectory. It is also well adapted to multi-blade cases as it is possible to manage overset mesh trajectories independently of each other. Finally, this approach is potentially less costly in computing time and more robust than a dynamic remeshing.

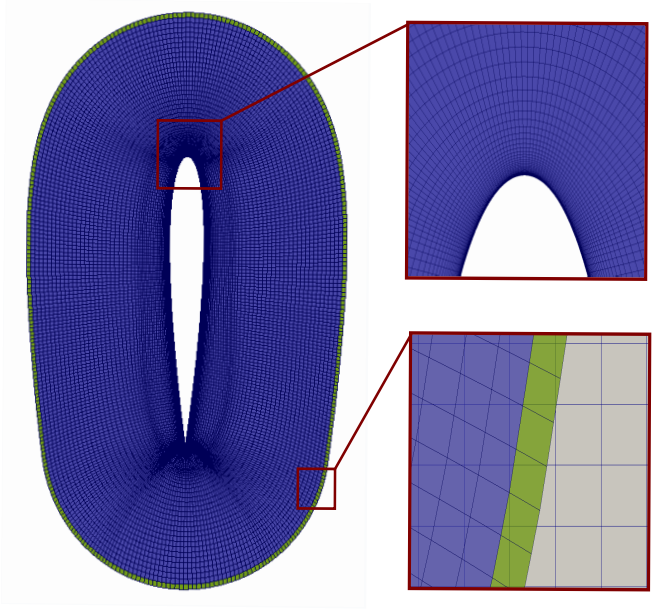

Fig. 5. Overset mesh with interpolated border cells in green.

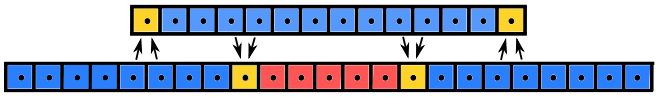

Fig. 6. 1D representation of the superimposition of an overset mesh (top) with the background mesh (bottom). The blue cells are calculated conventionally, the yellow cells are interpolated and the red cells are deactivated. The arrows represent the exchange of information by interpolation.

TABLE II
MESHES SIZE

Type of turbine	Cells in background mesh	Cells in overset meshes	Total
one-blade	136×10^3	28×10^3	164×10^3
two-blade	136×10^3	56×10^3	192×10^3
three-blade	136×10^3	84×10^3	220×10^3

Number of cells for turbine simulations with different number of blades and their distribution between background and overset meshes

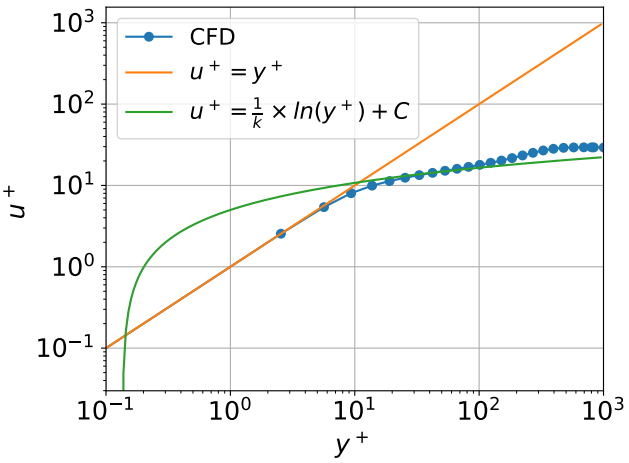

Fig. 7. Velocity profile scaled on the top surface of a blade at $0.3c$ from the leading edge at an angle of attack α=15°and a $Re = 7 \times 10^5$ (blue dots correspond to u^+ values at the cell centroid).

C. Verification

1) Space discretization convergence: The mesh convergence study was carried out for a classical non-overset mesh on a fixed blade at $Re = 7 \times 10^5$. The cells density according to the chord and according to the direction normal to the blade surface were multiplied until reaching a plateau on the value of the quantities of interest, namely the lift and drag coefficients. The retained mesh size divides the blade into 364 cells. The thickness of the cells attached to the profile ensures a $y^+ \sim 2$ in their centre. Thus, at least one cell of the mesh is located in the viscous sublayer (fig. 7).

The background mesh is composed of 136×10^3 cells and each overset mesh of 28×10^3 cells. The total number of cells for each simulation is summarised in Table II. The smallest cells in the background mesh are located in the area where the blades are moving. The ratio between the size of the background mesh cells in this area and the size of the cells at the overset boundary is $\Delta x_{background}/\Delta x_{overset} = 1.58$. The closer this ratio is to 1, the more accurate the interpolation between the meshes is. Thus, the mesh size ratio employed allows a correct interpolation while limiting the number of cells in the background mesh.

The simulations are run sequentially. Indeed, the implementation of solvers with overset meshes in OpenFOAM is relatively recent. The parallelization of this type of simulation was observed in this study to bring little or no time savings, at least on the cluster configuration used.

2) Time step convergence: To ensure that convergence in time step is achieved, the average power coefficient during the 12th blade revolution is calculated on a one-blade turbine case with $c/r = 0.8$ and $\lambda = 4$ with different time steps. The results are presented in Table III. For the rest of the study, the time step is chosen so as to have 1200 time steps per revolution.

To evaluate the cycle-to-cycle convergence of the simulations, the evolution of the average power coefficient over each cycle is considered. After 25 turbine revolutions, a variation of less than 1% is obtained for most of the simulations, with the exception of some low efficiency cases. The worst convergence is 3% variation in $\overline{C_p}$ between the last two cycles.

TABLE III
AVERAGE POWER COEFFICIENT $\overline{C_p}$

Time steps per cycle	$\overline{C_p}$	Variation with a time step twice as small
600	0.268	-
1200	0.298	9.7%
2400	0.303	1.7%

Average Cp during the 12th blade revolution of a one-blade turbine with $c/r = 0.8$ and $\lambda = 4$.

D. Validation

The validation of the numerical simulation results cannot be done by direct comparison with experimental results of the bi-axial turbine as it has not yet been

experimentally tested. Therefore, we choose to validate the simulations by comparison with a more classical case of a pitching airfoil. In this configuration a NACA 0012 airfoil oscillates with respect to an axis located at $c/4$ from its leading edge. The angle of attack during its sinusoidal oscillation is given by equation (5).

$$\alpha(t) = \alpha_0 + \Delta_\alpha sin(\omega t) \tag{5}$$

This time varying angle of attack is a common feature with the bi-axial turbine. It is a case that has been studied both experimentally by Lee [16] and numerically in particular by Gharali [17] and Delafin [18]. The overset mesh method was used in the present study with very similar characteristics to the turbine simulations and a slightly smaller background mesh. The overset mesh in this study and those in the bi-axial turbine simulations have the same O-grid topology. In both cases, the blade is discretized into 364 elements and the thickness of the first cell on the airfoil is defined in order to have $y^+_{max} \sim 1$. The numerical parameters are the same as in the turbine simulations (turbulence model, numerical schemes). A comparison of the instantaneous lift and drag coefficients obtained is shown in fig. 8. In the present study, the lift coefficient (C_L) is well predicted from $0°$ to $20°$ during the upstroke phase. The peak of C_L is predicted with a similar accuracy to the other simulations. In general, the simulation results presented in fig. 8 do not capture accurately the C_L in the downstroke phase and our results tend to underestimate a little more C_L in this phase. Regarding the drag coefficient (C_D), the present study gives results similar to the experiment close to the peak of C_D. Away from the peak, the present study predicts C_D with a similar accuracy to the other simulations (none of them being perfect). The simulations of Delafin [18] as well as those of the present study use a standard k-ω SST turbulence model. It assumes a fully turbulent boundary layer which is not the case in the experiment due to the low Reynolds number. This may explain some of the discrepancies between the experimental data and the simulation results (like the hysteresis at low AoA). The simulations of Gharali [17] use a k-ω SST model with a low-Reynolds number correction which accommodates the transitional regime and therefore may explain the slight hysteresis observed at low AoA.

The results presented show that the numerical set-up used in our study gives a similar level of accuracy to other published simulation results. The relatively poor agreement with the experimental data observed in the downstroke phase indicates that the turbine simulations at low tip speed ratios will have to be analyzed carefully in the semicircular motions. However, this validation process gives confidence in the results obtained in the linear regions and everywhere at high tip speed ratio, when angles of attack are below the stall angle.

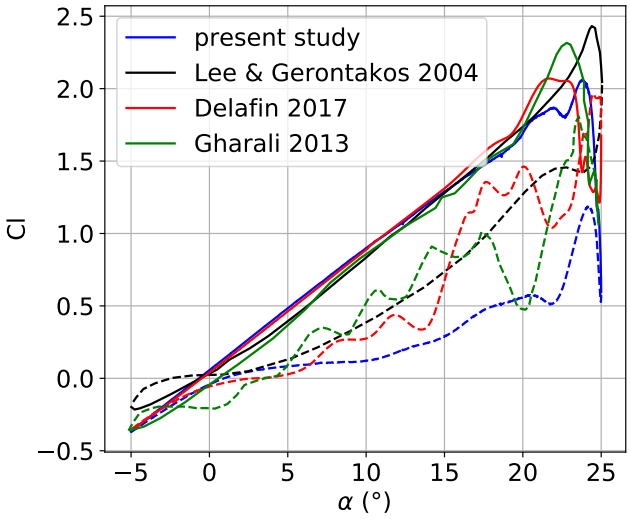

(a)

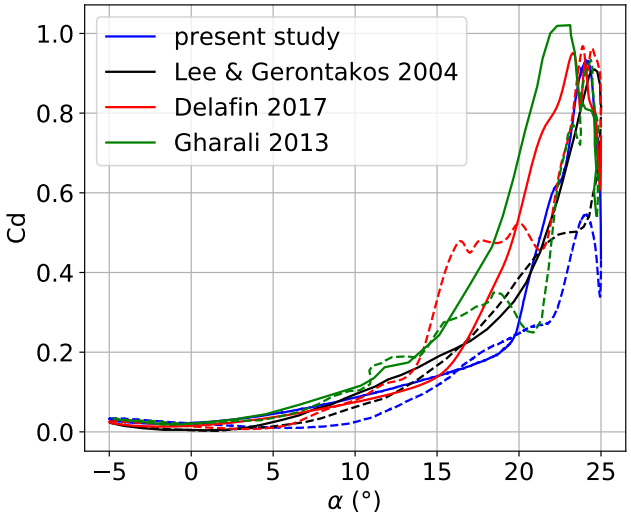

(b)

Fig. 8. Aerodynamic force coefficients comparison for α(t)=10°+15°$sin(\omega t)$ with $k = \omega c/2U_\infty = 0.1$ and $Re = 1.35 \times 10^5$. The continuous line corresponds to the increasing Angle of Attack (AoA) and the dashed line corresponds to the decreasing AoA.

IV. Results

A. Effect of solidity and blade number on performance

For each turbine configuration, a mean power coefficient curve as a function of the λ is plotted. This bell-shaped curve gives the optimum λ (λ_{opt}) for each configuration. A prototype of turbine equipped with a pulley speed control system would allow the turbine to always operate at this λ_{opt}. Conversely, if the turbine is designed with a constant drive speed, the hydraulic efficiencies achieved as a function of the upstream fluid speed can be deduced from a curve of mean C_p versus λ.

A first set of simulations of single-blade turbines with different chord sizes allows to study the influence of the solidity parameter on the performances (fig. 9). The dashed lines correspond to the values obtained in the penultimate cycle, the solid lines correspond to the values of the last cycle. The fact that both continuous and dashed lines are almost perfectly superimposed

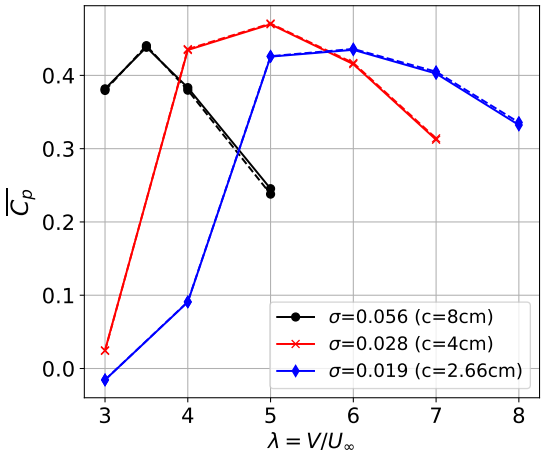

Fig. 9. Mean C_p as a function of λ for one-blade turbines with different solidity values.

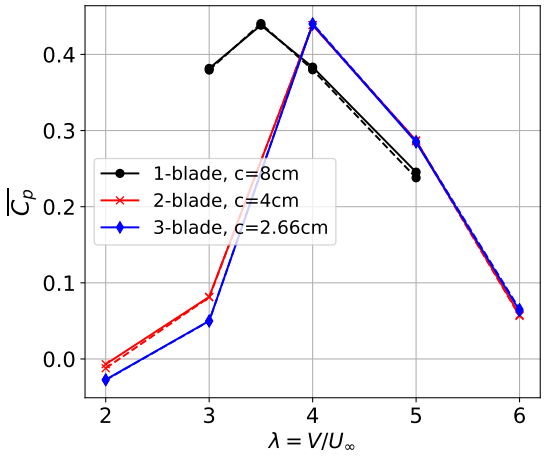

Fig. 10. Mean C_p as a function of λ for iso-solidity σ=0.056 turbine with different numbers of blades.

indicates that the convergence in number of turbine cycles is reached. It can be seen that λ_{opt} decreases as the solidity increases. This is an expected result as this phenomenon occurs for other types of turbine with horizontal or vertical axes [19], [20]. It also appears that $\sigma = 0.028$ leads to a higher peak of $\overline{C_p}$ than the two other cases. A maximum efficiency $\overline{C_p} = 0.47$ is then achieved with a single-blade turbine. It is noted that a lower solidity will give a lower maximum $\overline{C_p}$ but the performance curve as a function of λ will be flatter. These solidity-induced effects on turbine performance curve have been observed in the case of the Darrieus turbine by Paraschivoiu [19].

A second simulation set is launched to study the effect of the number of blades at iso-solidity (σ = 0.056) on the efficiency (fig. 10). The 2- and 3-blade cases give very close and even perfectly similar power coefficients for $\lambda \geq 4$. Again, this is an expected result that can be found for example in the case of Darrieus turbines [20]. The difference observed at lower λ could be linked to Reynolds effects. On the other hand, the performance obtained with an 8cm chord does not coincide with the other two configurations. The difference could be explained by the effect of the c/r ratio on the dynamics of the flow in the turns. Indeed, in the turns the blade sees a curved flow. This induces a greater camber and virtual incidence as the c/r ratio is greater. With $c = 8cm$, this ratio $c/r = 0.8$ is a rather extreme case and rarely encountered in the literature.

B. Influence of the number of blades on the instantaneous power coefficient

In this section, the evolution of the instantaneous power coefficient during a blade revolution is studied. To this purpose, a position parameter, noted "s" and varying from 0 to 1, is introduced (fig. 11). It allows to locate the blade along its trajectory. By convention, $s = 0$ when the link-point A close to the leading edge starts its downward vertical translation.

The instantaneous power coefficient of a single-blade turbine with chord $c/r = 0.4$ and λ=5, corresponding to the maximum $\overline{C_p}$, is shown in fig. 12. At $t/T = 0$,

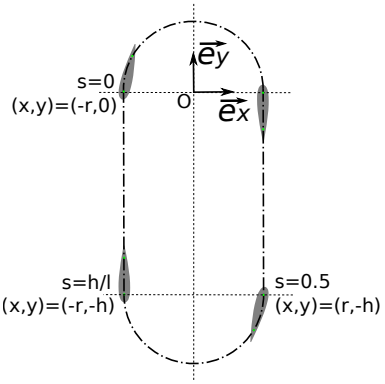

Fig. 11. Position parameter s for different blade positions and associated coordinates of point A.

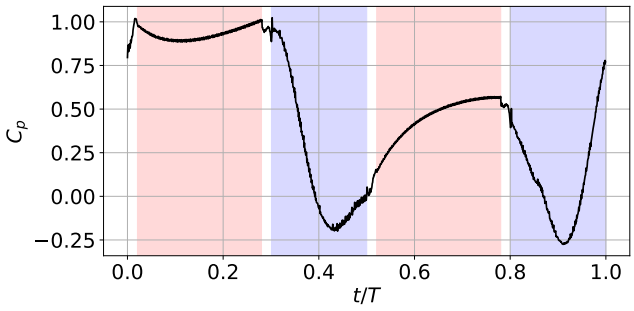

Fig. 12. Instantaneous C_p for the one-blade turbine with $c/r = 0.4$ and $\lambda = 5$. Red areas correspond to the translation motion. Blue areas correspond to the rotation motion.

the blade position parameter is $s = 0$. The downstream translation is the part of the trajectory where the blade receives the most power from the flow. During a part of the lower turn, the Cp becomes momentarily negative before becoming positive and gradually increasing again during the upward downstream translation. However, the power captured during the downstream translation remains significantly lower than the power captured during the upstream translation. This is due to the decrease in the flow velocity of the fluid as a result of wake effects (fig. 13).

Due to the large variation of the instantaneous C_p during a cycle, two turbine configurations with the

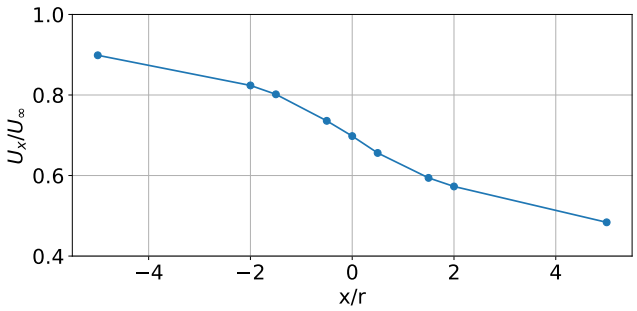

Fig. 13. Evolution of the mean streamwise velocity for the one-blade turbine with $c/r = 0.4$ and $\lambda = 5$.

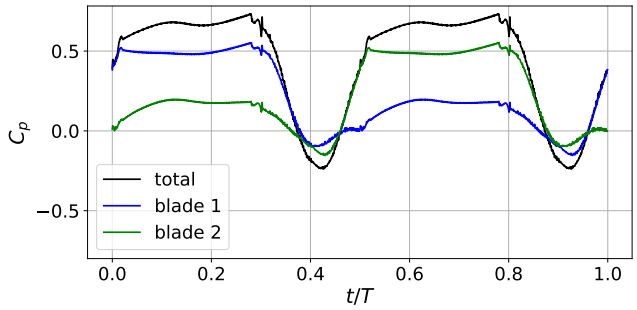

Fig. 14. Instantaneous C_p for 2-blade turbine with $c/r = 0.4$ and $\lambda = 4$.

same mean C_p can hide quite different behaviours. For example, fig. 14 shows the instantaneous C_p of a two-blade turbine with $c/r = 0.4$ and $\lambda = 4$. At $t/T = 0$, the position parameter of blade 1 is $s_1 = 0$, and the position parameter of blade 2 is $s_2 = 0.5$. Therefore, both blades will be in translation or rotation simultaneously. So the variation of the total C_p is more important than the variation of C_p received by each blade.

The instantaneous C_p of a case with the same overall efficiency but with a chord such that $c/r = 0.266$ and in a 3-blade configuration is plotted in fig. 15. At $t/T = 0$, the position parameter of blade 1 is $s_1 = 0$, it is $s_2 = 1/3$ for blade 2 and $s_3 = 2/3$ for blade 3. This time, the phase shift between the blades results in an instantaneous C_p that is always positive and varies much less around its mean value. The instantaneous $\overline{C_p}$ of a single blade in both 2- and 3-blade configurations (fig. 14 and fig. 15, respectively) follows the same behavior. Most of the energy is harnessed in the upstream part of the turbine and the downstream translation only generates a slightly positive $\overline{C_p}$.

C. Different flow regimes

In this section, we are interested in the influence of λ on the nature of the flow around the blades and therefore the performance of the turbine. The instantaneous C_p of a single-blade turbine with $c/r = 0.4$ is plotted for different values of λ in fig. 16. The curves are similar at $\lambda = 4$ and $\lambda = 5$. The case $\lambda = 3$ shows a more chaotic evolution, corresponding to a much lower mean C_p. This phenomenon can be explained by a change in the nature of the flow around the blade. The pressure on the blade surface and the vorticity

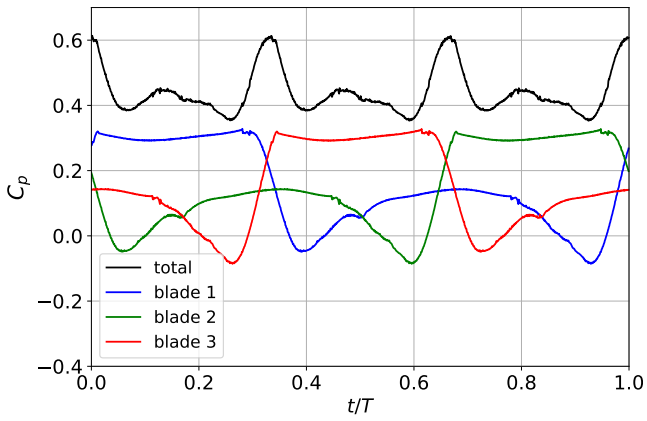

Fig. 15. Instantaneous C_p for 3-blade turbine with $c/r = 0.266$ and $\lambda = 4$.

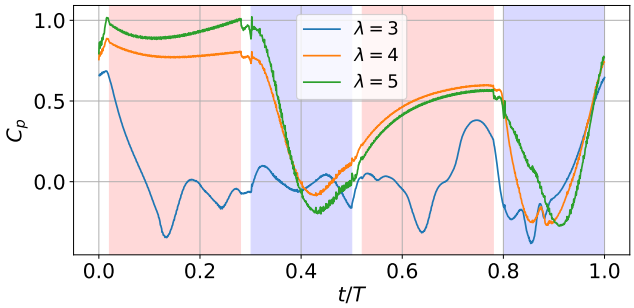

Fig. 16. Instantaneous C_p for one-blade turbine with $c/r = 0.4$.

field near the blade at different times in the cycle are represented in fig. 17 and fig. 18 for $\lambda = 3$ and $\lambda = 4$, respectively. The areas of overpressure on the blade are shown in red, the areas of depression in blue. The black arrows correspond to the forces transmitted by the blade to the chain at points A and B. If the arrows representing the forces are not visible it is because they are so small that they are hidden by the points of application of these forces (red point for A and blue point for B). This is notably the case for $\lambda = 3$ and $s = 0.4$. The scales of pressures and forces are the same in fig. 17 and fig. 18. At $\lambda = 4$, the angle of attack between the relative speed of the fluid and the blade is inferior to the stall angle during most of its trajectory. On the other hand, the blade stalls over most of its trajectory at $\lambda = 3$, which produces eddies that disturb the flow and decrease the performance.

During the lower turn, power coefficients for $\lambda = 4$ and $\lambda = 5$ vary similarly (fig. 16). In the two cases the flow is nearly attached (not shown here for $\lambda = 5$). The greater negative peak for $\lambda = 5$ could come from a greater friction due to a higher blade velocity. During the upper turn, the C_p variations for $\lambda = 4$ and $\lambda = 5$ are no longer similar. This could come from the flow detachment at $\lambda = 4$ (fig. 18), which is not present for $\lambda = 5$ (not shown here). In the last case, the negative peak is higher than for the lower turn probably because the relative velocity is higher.

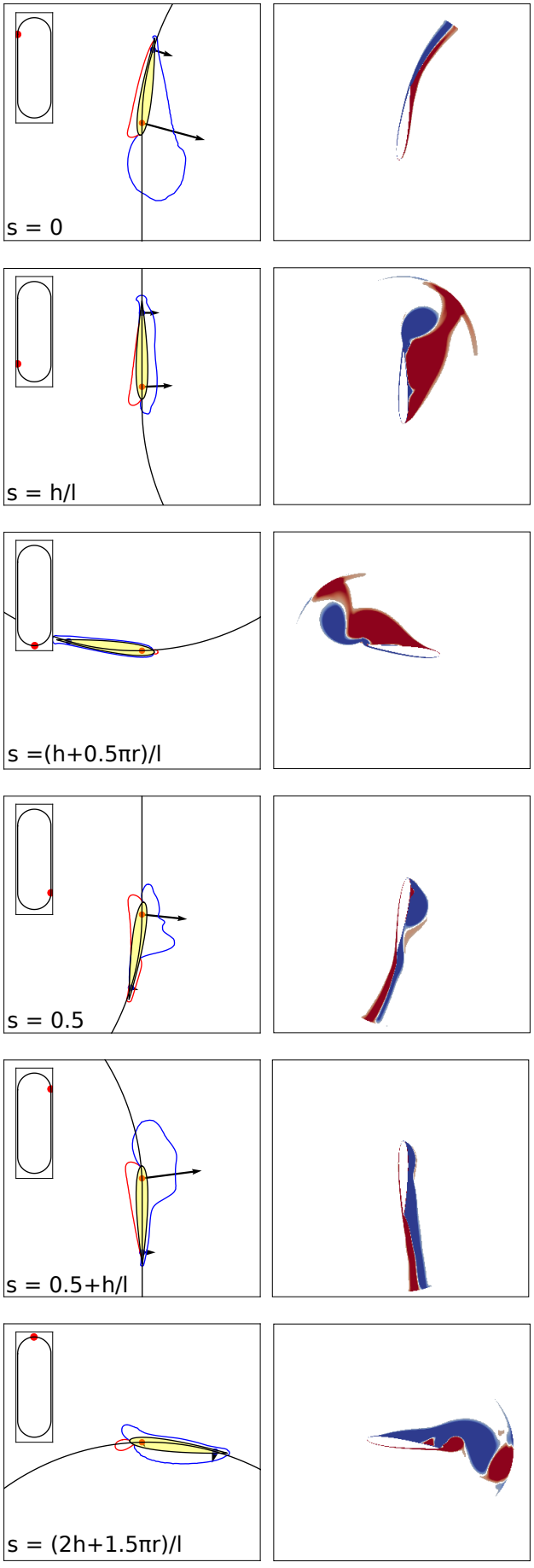

Fig. 17. Pressure distribution over the blade surface plus vectors of the force exerted by the blade on the chain (left) and vorticity field (right) for a one-blade turbine with $c/r = 0.4$ and $\lambda = 3$. The scales of force vectors and pressure are the same as in fig. 18.

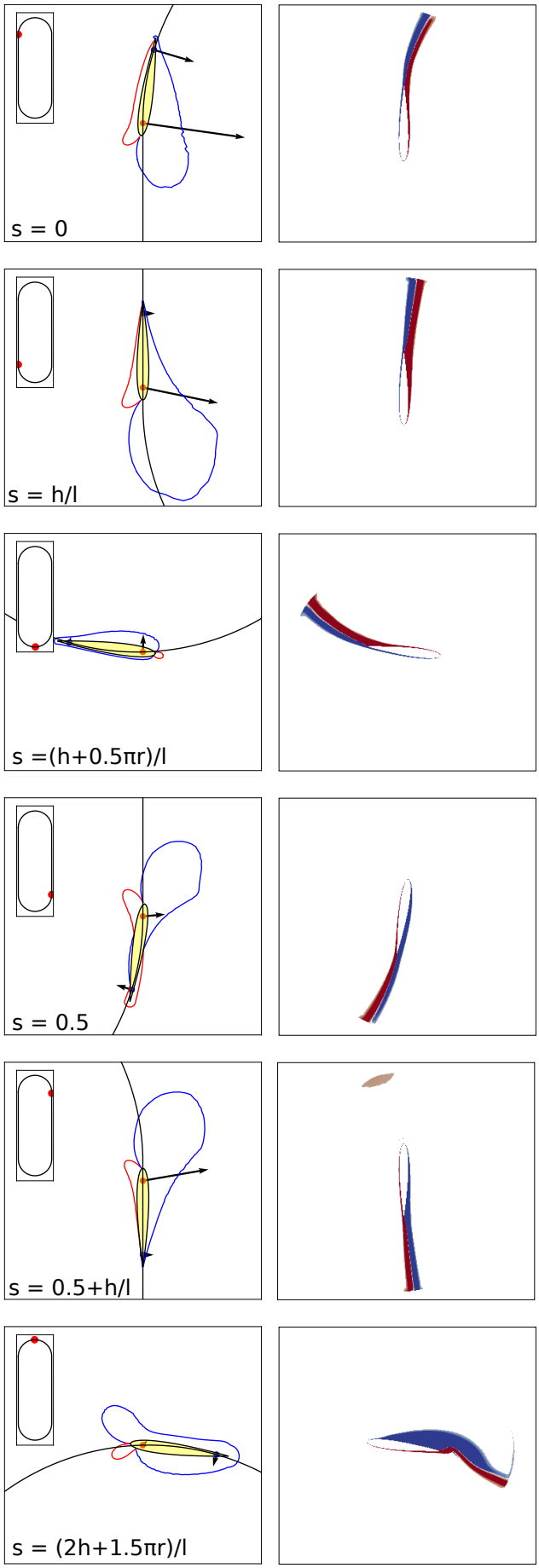

Fig. 18. Pressure distribution over the blade surface plus vectors of the force exerted by the blade on the chain (left) and vorticity field (right) for a one-blade turbine with $c/r = 0.4$ and $\lambda = 4$. The scales of force vectors and pressure are the same as in fig. 17.

V. Conclusion

The bi-axial turbine concept seems to be able to achieve interesting efficiencies. 2D overset mesh simulations of one-blade, two-blade and three-blade turbines with different chord lengths have been performed using the OpenFOAM solver. This allowed to highlight recurrent behaviour that can be found with other types of turbines, notably the Darrieus turbines. For example, it appears that, all other things being equal, increasing the solidity causes a decrease in the optimal λ. On the other hand, turbines with different blade numbers but the same solidity will have very similar power coefficient versus λ curves. This behaviour is observed for $c/r \leq 0.4$ but it ceases to be true when the c/r ratio becomes too high (here $c/r = 0.8$), perhaps due to the effects of virtual camber in turns.

Finally, the observation of the instantaneous power coefficient over a revolution cycle shows a difference in behaviour between two-blade turbines and three-blade turbines. Indeed, with the same solidity and the same average efficiency, the arrangement of the blades gives a momentary negative global coefficient for the two-blade turbines, whereas it always remains positive and is less fluctuating for a three-blade turbine.

References

[1] G. J. M. Darrieus, "Turbine having its rotatings shaft transverse to the flow of the current," U.S. Patent 1835018A, 1931.

[2] M. Worstell, "Aerodynamic Performance of the DOE/Sandia 17-m Diameter Vertical Axis Wind Turbine," Journal of Energy, p. 39–42, 1981.

[3] J. Dabiri, "Potential order-of-magnitude enhancement of wind farm power density via counter-rotating vertical-axis wind turbine arrays," Journal of Renewable and Sustainable Energy, vol. 3, no. 4, p. 043104, 2011. [Online]. Available: https://doi.org/10.1063/1.3608170

[4] H. Sutherland, D. Berg, and T. Ashwill, "A Retrospective of VAWT Technology," SANDIA, Tech. Rep. SAND2012-0304, 2012.

[5] V. Clary, T. Oudart, P. Larroudé, J. Sommeria, and T. Maître, "An optimally-controlled RANS Actuator force model for efficient computations of tidal turbine arrays," Ocean Engineering, vol. 212, p. 107677, 2020. [Online]. Available: http://www.sciencedirect.com/science/article/pii/S0029801820306703

[6] M. Shiono, K. Suzuki, and S. Kiho, "An Experimental Study of the Characteristics of a Darrieus Turbine for Tidal Power Generation," Electrical Engineering in Japan, vol. 132, pp. 781–787, 2000.

[7] P. G. Migliore, "Flow Curvature Effects on Darrieus Turbine Blade Aerodynamics," J. ENERGY, vol. 4, 1980.

[8] E. Hau, Wind Turbines Fundamentals, Technologies, Application, Economics. Springer, 2013.

[9] P. Delafin, F. Deniset, J. Astolfi, and F. Hauville, "Performance Improvement of a Darrieus Tidal Turbine with Active Variable Pitch," energies, 2021.

[10] W. McKinney and J. DeLauriert, "The Wingmill: An Oscillating-Wing Windmill," J. ENERGY, vol. 5, 1981.

[11] T. Kinsey and G. Dumas, "Computational Fluid Dynamics Analysis of a Hydrokinetic Turbine Based on Oscillating Hydrofoils," Journal of Fluids Engineering, vol. 134, 2012.

[12] G. Naccache and M. Paraschivoiu, "Development of the Dual Vertical Axis Wind Turbine Using Computational Fluid Dynamics," Journal of Fluids Engineering, vol. 139, 2017.

[13] ——, "Parametric study of the dual vertical axis wind turbine using CFD," Journal of Wind Engineering & Industrial Aerodynamics, vol. 172, 2017.

[14] F. R. Menter, "Two-Equation Eddy-Viscosity Turbulence Models for Engineering Application," American Institute of Aeronautics and Astronautics, vol. 32, 1994.

[15] F. R. Menter, M. Kuntz, and R. Langtry, "Ten Years of Industrial Experience with the SST Turbulence Model," Turbulence, Heat and Mass Transfer 4, 2003.

[16] T. Lee and G. Gerontakos, "Investigation of flow over an oscillating airfoil," Journal of Fluid Mechanics, vol. 512, pp. 313–341, 2004.

[17] K. Gharali and D.-A. Johnson, "Dynamic stall simulation of a pitching airfoil under unsteady freestream velocity," Journal of Fluids and Structures, vol. 42, pp. 228–244, 2013.

[18] P.-L. Delafin, T. Nishino, A. Kolios, and L. Wang, "Comparison of low-order aerodynamic models and rans cfd for fullscale 3d vertical axis wind turbines," Renewable Energy, vol. 139, 2017.

[19] I. Paraschivoiu, Wind Turbine Design: With Emphasis on Darrieus Concept. Polytechnic International Press, 2002.

[20] P.-L. Delafin, T. Nishino, L. Wang, and A. Kolios, "Effect of the number of blades and solidity on the performance of a vertical axis wind turbine," Journal of Physics: Conference Series, vol. 753, p. 022033, sep 2016. [Online]. Available: https://doi.org/10.1088%2F1742-6596%2F753%2F2%2F022033